Communication

Spontaneous Osteogenic Differentiation of Human Mesenchymal Stem Cells by Tuna Bone-Derived Hydroxyapatite Composites with Green Tea Polyphenol-Reduced Graphene Oxide

Moon Sung Kang [1,†], Rowoon Park [1,†], Hyo Jung Jo [1], Yong Cheol Shin [2], Chang-Seok Kim [1,3], Suong-Hyu Hyon [4], Suck Won Hong [1,3,*], Junghwan Oh [5,6,7,*] and Dong-Wook Han [1,8,*]

[1] Department of Cogno-Mechatronics Engineering, College of Nanoscience and Nanotechnology, Pusan National University, Busan 46241, South Korea; mskang7909@gmail.com; rowoon.p153@gmail.com; lisa0245@naver.com; ckim@pusan.ac.kr
[2] Department of Inflammation and Immunity, Lerner Research Institute, Cleveland Clinic, OH 44195, USA; shiny2@ccf.org
[3] Engineering Research Center for Color-Modulated Extra-Sensory Perception Technology, Pusan National University, Busan 46241, South Korea
[4] BMG Inc., Kyoto 601-8023, Japan; biogen@bmg-inc.com
[5] Industry 4.0 Convergence Bionics Engineering, Pukyong National University, Busan 48513, South Korea
[6] Department of Biomedical Engineering, Pukyong National University, Busan 48513, South Korea
[7] Ohlabs Corporation, Busan 48513, South Korea
[8] BIO-IT Fusion Technology Research Institute, Pusan National University, Busan 46241, South Korea
* Correspondence: swhong@pusan.ac.kr (S.W.H.), jungoh@pknu.ac.kr (J.O.), nanohan@pusan.ac.kr (D.-W.H.)
† These authors equally contributed to this work.

Abstract: In recent years, bone tissue engineering (BTE) has made significant progress in promoting the direct and functional connection between bone and graft, including osseointegration and osteoconduction, to facilitate the healing of damaged bone tissues. Herein, we introduce a new, environmentally friendly, and cost-effective method for synthesizing reduced graphene oxide (rGO) and hydroxyapatite (HAp). The method uses epigallocatechin-3-*O*-gallate (EGCG) as a reducing agent to synthesize rGO (E-rGO), and HAp powder is obtained from Atlantic bluefin tuna (Thunnus thynnus). The physicochemical analysis indicated that the E-rGO/HAp composites had exceptional properties for use as BTE scaffolds, as well as high purity. Moreover, we discovered that E-rGO/HAp composites facilitated not only proliferation, but also early and late osteogenic differentiation of human mesenchymal stem cells (hMSCs). Our work suggests that E-rGO/HAp composites may play a significant role in promoting the spontaneous osteogenic differentiation of hMSCs, and we envision that the E-rGO/HAp composites could serve as promising candidates for BTE scaffolds, stem cell differentiation stimulators, and implantable device components due to their biocompatible and bioactive properties. Overall, we suggest a new approach for developing cost-effective and environmentally friendly E-rGO/HAp composite materials for BTE application.

Keywords: bone tissue engineering; hydroxyapatite; reduced graphene oxide; human mesenchymal stem cell; osteogenic differentiation

1. Introduction

To date, many patients have experienced irreversible bone damage due to traumatic injuries, tumors, degenerative diseases, and bacterial or viral infections [1, 2]. However, the supply of autograft and allograft is insufficient to meet clinical demands, and most artificial grafts do not provide proper cell-matrix interactions or mechanical synchronization with natural tissues leading

 doi:10.20944/preprints202305.0126.v1

to weakening of original tissues by the shear stress and friction, or necrosis and inflammatory reactions [3]. Bone tissue engineering (BTE) scaffolds have emerged as a promising approach to rehabilitate bone losses by filling damaged cavities and facilitating native wound healing [4]. BTE scaffold development involves cytocompatible materials that are similar to those found in native bones, creating a microenvironment that promotes cellular adhesion, migration, proliferation, and osteogenic differentiation [5, 6]. As a result, BTE studies use various biomaterials to support structural integrity and facilitate osseointegration, which is the direct and functional connection between bone and graft, as well as osteoconduction, which is the growth of new bone on the graft's surface [7, 8].

Hydroxyapatite ($Ca_{10}(PO_4)_6(OH)_2$, HAp) is a type of mineral apatite that contains hydroxyl, which can be synthesized using various methods including precipitation [9], hydrothermal [10], mechano-chemical [11, 12], polymer-assisted [13], and sol-gel techniques [14]. Especially, due to its exceptional biocompatibility, osteoconductivity, and osteoinductivity, HAp have been highlighted for the orthopedic application such as bone defect fillers, bone graft substitutes, coating material of graft surface, or extender [15, 16]. Because the crystalline phase of natural bone is mostly composed of HAp (approximately 65 w/w %), its usage as BTE scaffolds assures strong affinity to host bone matrix and provide native niche to promote revelation of osteogenic phenotypes. Moreover, having a stoichiometric calcium-to-phosphorus ratio of 1:67 (w:w), HAp is the most stable and least soluble form of calcium phosphate composite in nature [17]. Especially, the nature-derived HAp is known to exhibits more bioactivity compared to chemically synthesized ones [18, 19]. The superior bioactivity of nature-derived HAp comes from nanometric crystal size and presence of essential ions for bone morphogenesis such as Mg^{2+}, K^+, Na^+, and Sr^{2+} [18]. There are several kinds of HAp sources including eggshells, corals, fish bones, bovine or porcine bones, and even biowastes [19-24]. Especially, fish bone-derived HAp is apparently safer than that of mammalian bones by avoiding the risk of side effects such as bovine spongiform encephalopathy (BSE) and the foot-and-mouth disease (FMD) [25]. Moreover, recycling of the tremendous burden of fish wastes can lead to the environmental advantages [26]. In this context, the Atlantic bluefin tuna (*Thunnus thynnus*), which is a species of tuna in the family *Scombridae* found widely in the northern Pacific Ocean, was adopted as HAp source [27]. The thermal calcination was used for the isolation of HAp from the tuna bone, which is commonly used HAp extraction process [28].

However, the low mechanical strength of normal HAp ceramics restricts its use mainly only to low load-bearing applications [29]. To overcome this issue, we incorporated reduced graphene oxide (rGO) nanosheets into HAp to increase the mechanical strength and osteogenic capability. The rGO is prepared by chemical or thermal reduction of graphene oxide (GO) to induce structural defects while maintaining the oxidized groups [30]. The potential of rGO has been investigated as a prominent promoter for osteogenic differentiation of human mesenchymal stem cells (hMSCs) [31]. The residual oxygen-containing functional moieties on the basal planes and edges of rGO actively absorb and interact with surrounding biomolecules to modulate cell behaviors [32]. Also, our previous studies have demonstrated on the clear cell modulating effects of rGO such as proliferation and osteogenesis by utilizing graphene-based nanomaterials [33]. Furthermore, we utilized abundant polyphenols found in green tea named epigallocatechin-3-*O*-gallate (EGCG) to synthesize the rGO nanosheets, which is named E-rGO [34]. The EGCG is known to be effective and mild reducing agent for graphene materials, furthermore, presents π-conjugated structure which interacts with graphene sheets and helps disaggregation of graphene bundles to provide stable dispersions [35, 36].

This study involved the development of a new composite material named E-rGO/HAp composites by conjugating EGCG-reduced rGO with tuna bone-derived HAp. The physicochemical properties of tuna bone-derived HAp were found to be similar to those of pristine HAp. The morphology, chemical composition, and zeta potential of E-rGO/HAp were elucidated. Subsequently, cellular behaviors such as proliferation, ALP activity, and mineralization nodules formation were evaluated on E-rGO/HAp substrates.

2. Materials and Methods

Preprints (www.preprints.org) | NOT PEER-REVIEWED | Posted: 3 May 2023 doi:10.20944/preprints202305.0126.v1

2.1. Preparation of E-rGO/HAp composites

2.1.1. Preparation of E-rGO and tuna bone-derived HAp

The technique for converting GO into rGO involved heating it in a solution containing EGCG (BMG Inc., Kyoto, Japan). The procedure began by diluting the commercial GO solution (Sigma-Aldrich, St. Louis, MO) to a concentration of 1 mg mL^{-1} in sterilized deionized (DI) water. Next, EGCG powder was added to the solution to achieve a final concentration of 10 mg mL^{-1}. As shown in Fig. 1a, the resulting mixture was sealed tightly and heated at 80°C for 8 h. After heating, the mixture was sonicated for 1 h and gradually cooled down in water over a period of 12 h. The Atlantic bluefin tuna (*Thunnus thynnus*) bone (Dongwon, Seoul, South Korea) was cleansed thoroughly by washing with DI water to remove organic components. The bones were then boiled for 20 mins and treated with 0.1 N NaOH, followed by rinsing with DI water. To purify the HAp, the bones were calcined at 800°C (Fig. 1b). As the control, the commercially available water-soluble HAp powder (Dentis Co., Ltd., Daegu, South Korea) was used.

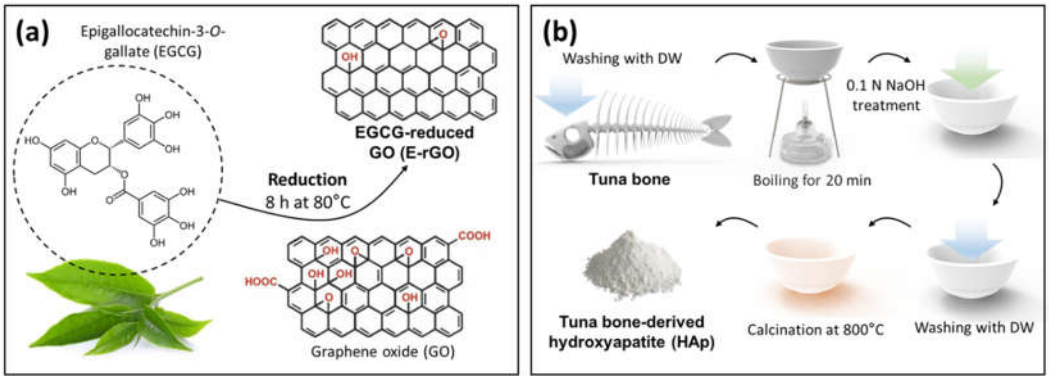

Figure 1. Schematic diagram of preparation of E-rGO and tuna bone-derived HAp. (a) Preparation process of E-rGO reduced by EGCG. (b) Procurement process of HAp from Atlantic bluefin tuna (*Thunnus thynnus*) bone.

2.1.2. Synthesis of E-rGO/HAp composites

To prepare E-rGO/HAp composites, as-prepared 1 mg mL^{-1} E-rGO solution was sonicated for 2 h and then mixed with a 1 mg mL^{-1} tuna-derived HAp powders suspended in DI water with the weight ratio of 1:1. Colloidal dispersions of E-rGO and HAp were vigorously mixed using a vortex for 10 min and slowly air-dried at 25°C overnight, which results in the E-rGO/HAp composites.

2.2. Physicochemical characterizations

2.2.1. Physicochemical characterizations of tuna bone-derived HAp

The tuna bone-derived HAp was analyzed for its composition using Fourier-transform infrared (FT-IR) spectroscopy attached with Spectrum GX instrument (PerkinElmer Inc., Waltham, MA). During FT-IR analysis, the spectra were recorded in absorption mode and were scanned 16 times within the wavelength range of 500—4000 cm^{-1} with a resolution of 4.0 cm^{-1}. To determine the crystalline structure of the HAp, X-ray diffraction (XRD) patterns were obtained using an X-ray diffractometer (Empyrean series 2, PANalytical, Almelo, Netherlands). The HAp was scanned in the continuous scan mode using Cu-Kα radiation with a wavelength of λ = 0.154 nm, at a voltage of 40 kV and a current of 30 mA. The scanning was performed at a temperature of 25°C in the 2θ range of 10–60°, with a scan rate of 2θ = 2° min^{-1}. Thermogravimetry and differential scanning calorimetry (TG-DSC, STA 449 F1 Jupiter, NETZSCH-Feinmahltechnik GmbH, Selb, Germany) measurements were used to conduct a thermal analysis on both the pristine HAp and tuna-derived HAp. The samples were heated to 800°C at a rate of 5°C min^{-1} in the presence of a helium gas flow, while the

Preprints (www.preprints.org) | NOT PEER-REVIEWED | Posted: 3 May 2023 doi:10.20944/preprints202305.0126.v1

released gases were analyzed by quadrupole mass spectrometry (403 Aëolos, NETZSCH-Feinmahltechnik) simultaneously.

2.2.2. Physicochemical characterizations of E-rGO/HAp composites

The surface morphology of the prepared E-rGO/HAp composites were observed by field emission FE-SEM (Carl Zeiss Supra 40VP, Oberkochen, Germany) at an accelerating voltage of 15 kV. The energy dispersive X-ray spectrometer (EDS) of E-rGO/HAp composites was assessed using 10 images taken in random surfaces at 2000 × magnification. Elemental mapping was performed for phosphorus, calcium, and carbon with 10 mm^2 window size, detectable range of 4Be-92U with resolution of MnKα (131eV@100,000 count per second). The Raman spectra of the E-rGO/HAp composites were obtained using a Raman spectroscopy system (Ramboss 500i, Dongwoo Optron Co., Ltd., Gwangju, South Korea) that included a charge-coupled device camera (iDusDV420A-OE, Andor Technology, Belfast, Ireland) and a precise motorized stage (SGSP 20–85, Sigma Koki Co., Ltd., Tokyo, Japan). An Ar-ion laser with a wavelength of 532 nm (LasNova 50, LASOS, Jena, Germany) was focused onto the sample by means of a water immersion objective lens (× 60 magnification, numerical aperture of 1.2 UPlanSApo, Olympus, Tokyo, Japan) and the resulting signal was analyzed with a monochromator (Monora500i, Dongwoo Optron). The laser power was set at 5 mW at 532 nm and was attenuated by a 50% neutral density filter at the objective. The Raman spectra were collected over a range of 1200—2000 cm^{-1}. Surface potentials of HAp, E-rGO, and E-rGO/HAp were measured by a zetasizer (Nano ZS, Malvern Instruments, Worcestershire, UK). While measuring the zeta-potential, the pH value of each suspension (10 μg mL^{-1}) was monitored and maintained at pH 7.0.

2.3. Cell culture conditions

Lonza (Walkersville, MD, USA) was the source of hMSCs used in all experiments, with cells between passages 3 and 5 being utilized. To ensure they remained in an undifferentiated state, hMSCs were regularly cultured at 37°C under 5% CO_2 in a humidified atmosphere using MSC basal medium (Lonza), supplemented with 10% MSC growth supplement (Lonza), 2% L-glutamine, 0.1% GA-1000, and 1% antibiotic-antimycotic solution (Sigma-Aldrich), which contains 10,000 units of penicillin, 10 mg of streptomycin, and 25 μg of amphotericin B per mL. To induce osteogenic differentiation, hMSCs were instead cultured in α-Minimum Essential Medium (α-MEM) supplemented with 10^{-8} M dexamethasone (Abcam, Cambridge, UK), 0.2 mM ascorbic acid (Sigma-Aldrich), and 10 mM β-glycerolphosphate (Sigma-Aldrich).

2.4. Cell proliferation assay

To evaluate the impact of E-rGO/HAp composites on the proliferation of hMSCs, a cell counting kit-8 (CCK-8) assay was performed in accordance with the manufacturer's guidelines (Dojindo Laboratories, Kumamoto, Japan). A concentration of 10 μg mL^{-1}. of E-rGO/HAp composites were added to 48-well plates, and 1 × 10^4 cells mL^{-1} of hMSCs were then seeded on the plates for predetermined durations. After 1, 3, and 5 days of incubation, each sample was washed twice with DPBS and reacted with CCK-8 solution (diluted with DPBS at 1:9 v/v) for 2 h in a dark, humid environment at 37°C under 5% CO_2. The absorbance of each sample was measured at 450 nm using a microplate reader (Thermofisher scientific, Waltham, MA) at each time point.

2.5. Alkaline phosphatase (ALP) activity assay and alizarin red S (ARS) staining

To investigate the hMSCs' osteogenic differentiation, an ALP activity assay was conducted. The hMSCs were seeded at a concentration of 1 × 10^4 cells mL^{-1} on 48-well plates, and a 10 μg mL^{-1} of E-rGO/HAp was treated for 1, 7, 14, and 21 days. The conversion of p-nitrophenyl-phosphate to p-nitrophenol was measured to determine ALP activity using an ALP assay kit (Abcam, Cambridge, UK) according to the manufacturer's instructions. The absorbance at 405 nm was measured at each time point using a microplate reader. ALP activity was calculated by dividing the total amount of ρ-nitrophenol formation (μmol) by the reaction time (min) and sample volume (mL). To examine the

Preprints (www.preprints.org) | NOT PEER-REVIEWED | Posted: 3 May 2023 doi:10.20944/preprints202305.0126.v1

formation of extracellular calcium deposits of the cells, hMSCs were seeded at a concentration of 1 × 10^4 cells mL^{-1} on 48-well plates, and a 10 μg mL^{-1} of E-rGO/HAp was treated for 1, 7, 14, and 21 days. At each time point, the cells were washed twice with DPBS solution, fixed with 3.7% formaldehyde solution for 10 min, and then stained with 40 mM ARS dye (Sigma-Aldrich). The samples were then photographed with a digital camera (Olympus Optical Co., Ltd., Tokyo, Japan). To quantify the calcium deposits, the ARS dye was extracted from the stained cells by adding a 10% acetic acid solution and incubating the samples for 30 min with constant shaking at 80 rpm. A 10% ammonium hydroxide solution was then added to neutralize the aqueous solution of the ARS extracts, and the absorbance was measured at 405 nm using a microplate reader.

2.6. Statistical analysis

All variables were tested in three independent cultures for each experiment, which was repeated twice (n = 6). The quantitative data are expressed as the mean ± standard deviation. Before statistical analysis, the data were analyzed for the equality of variances using Levene's test. Multiple statistical comparisons were performed using the Bonferroni test after a preliminary one-way analysis of variance; the asterisks indicate statistical significance between groups (***$p < 0.001$ and ****$p < 0.0001$), while not significant differences were not noted.

3. Results and Discussion

To validate the chemical compositions of pristine HAp and tuna-derived HAp, FT-IR spectra were analyzed (Fig. 2a). On pristine HAp, the peak at 3568 cm^{-1} denotes ion stretching vibration of O-H bond in the hydroxyl group [37]. The broad peaks at 1099, 1041, and 966 cm^{-1} represent the asymmetric stretching P-O bond in the phosphate ion [37]. The sharp peaks at 638, 601, and 573 cm^{-1} denotes asymmetric bending vibration of P-O bond in phosphate ion [37]. On the other hand, characteristic peaks were observed in tuna-derived HAp compared to pristine HAp. The peaks at 1420 and 880 cm^{-1} denote asymmetric stretching and out of plane bending mode of C-O bond in carbonate ion, respectively [38]. The XRD method was used to analyze the structure of a tuna-derived HAp compared to pristine HAp (Fig. 2b). The sharp-shaped XRD peaks of tuna-derived HAp and pristine HAp indicate high crystallinity. The peak positions match the JCPDS (896438) and correspond with d-spacing values of 2.82 Å, 2.79 Å, and 2.72 Å indicating a hexagonal system with a primitive lattice, of which findings align with previous researches [37, 39]. Therefore, we confirmed the tuna-derived HAp was successfully synthesized without impurities having similar chemical characteristics of pristine HAp. Furthermore, we hypothesized that the plenty of oxygen-containing functional groups of tuna-derived HAp could facilitate cellular behaviors by anchoring serum proteins and growth factors, as well as enhancing cell-matrix interactions [40].

Preprints (www.preprints.org) | NOT PEER-REVIEWED | Posted: 3 May 2023 doi:10.20944/preprints202305.0126.v1

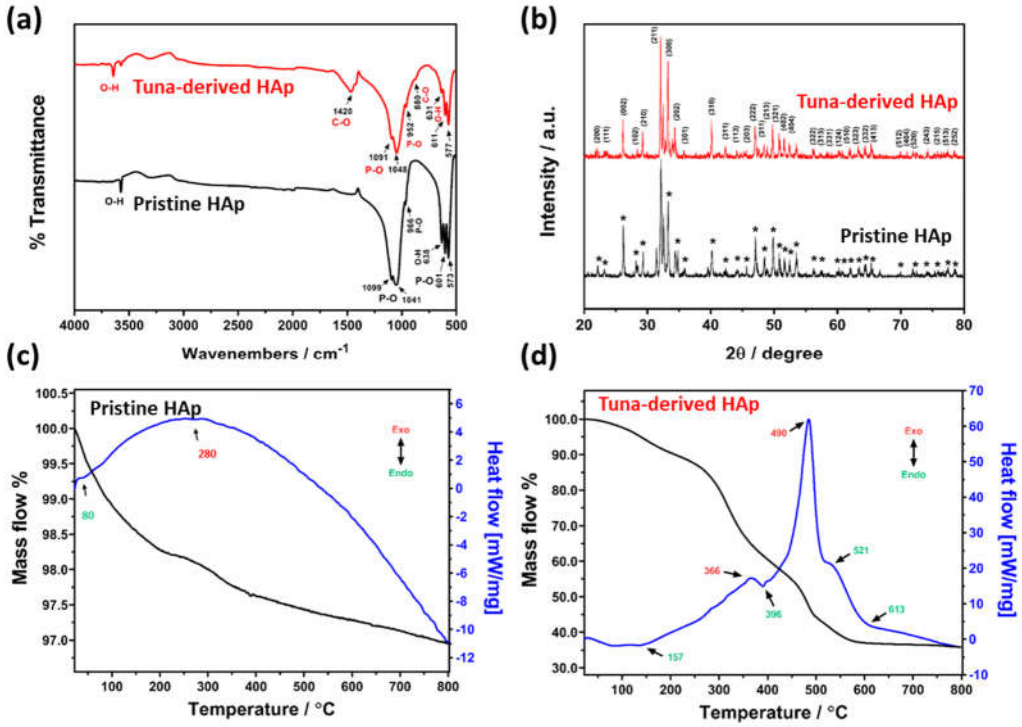

Figure 2. Physicochemical characterization of tuna-derived HAp compared to pristine HAp. (a) FT-IR and (b) XRD spectra of tuna-derived HAp and pristine HAp. TGA and DSC analysis of (c) pristine HAp and (d) tuna-derived HAp.

Figures 2c and 2d display the DSC analysis of both pristine HAp and tuna-derived HAp. The mass flow curve of pristine HAp exhibits three main steps. The first step, occurring between 20 to 200°C, shows a decrease in mass of around 1.7%, resulting from the evaporation of physically adsorbed water on the HAp surface. This step corresponds to the endothermic peak observed at approximately 60°C in the heat flow [41, 42]. The second step begins at around 250°C and ends at 380°C, causing a mass loss of roughly 0.7%, which can be attributed to the removal of chemically adsorbed water [41, 42]. The DSC curve is dominated by an exothermic broad band, which corresponds to a structural rearrangement on the crystal lattice. At approximately 700°C, continuous mass loss is observed due to the release of CO_3^{2-} that occupies the hydroxide or phosphate sites [43]. In contrast, the TG-DSC results of tuna-derived HAp indicate a significant mass loss and chemical transformation. The first significant mass loss of 4.8% was recorded at 160°C, which is associated with the massive dehydration of the sample and the elimination of bone structure and collagen components [44]. The tuna-derived HAp exhibits multi-stage losses up to 800°C, which can be attributed to the removal of CO_3, H_2O, and NH_3 content, suggesting the residual presence of matrix fibers organic compounds in the sample [45].

Preprints (www.preprints.org) | NOT PEER-REVIEWED | Posted: 3 May 2023 doi:10.20944/preprints202305.0126.v1

Next, the E-rGO/HAp was prepared as described in materials and methods section using the tuna-derived HAp. The SEM images of E-rGO/HAp indicates that both HAp NPs and E-rGO HAp have approximately 500 – 800 nm sizes and single or few-layered E-rGO sheets are adsorbed on the surface of HAp NPs (Fig. 3a). The EDS analysis showed that the E-rGO/HAp composites consist of 79.31% calcium and 16.90% phosphate from the HAp components, along with 3.79% carbon from the E-rGO (Fig. 3b). The EDS spectrum did not reveal any other impurities within the detection limit of the instrument, which confirms the E-rGO/HAP composites' purity, containing only Ca, P, and C elements. The semiquantitative analysis indicated a Ca/P molar ratio of approximately 4.69, which is significantly higher than the ratio observed in previous studies, typically around 1.66 [46]. This higher Ca ratio leads to the CaO phase becoming the dominant phase in the HAp that might enhance the osteoblast adhesion [47].

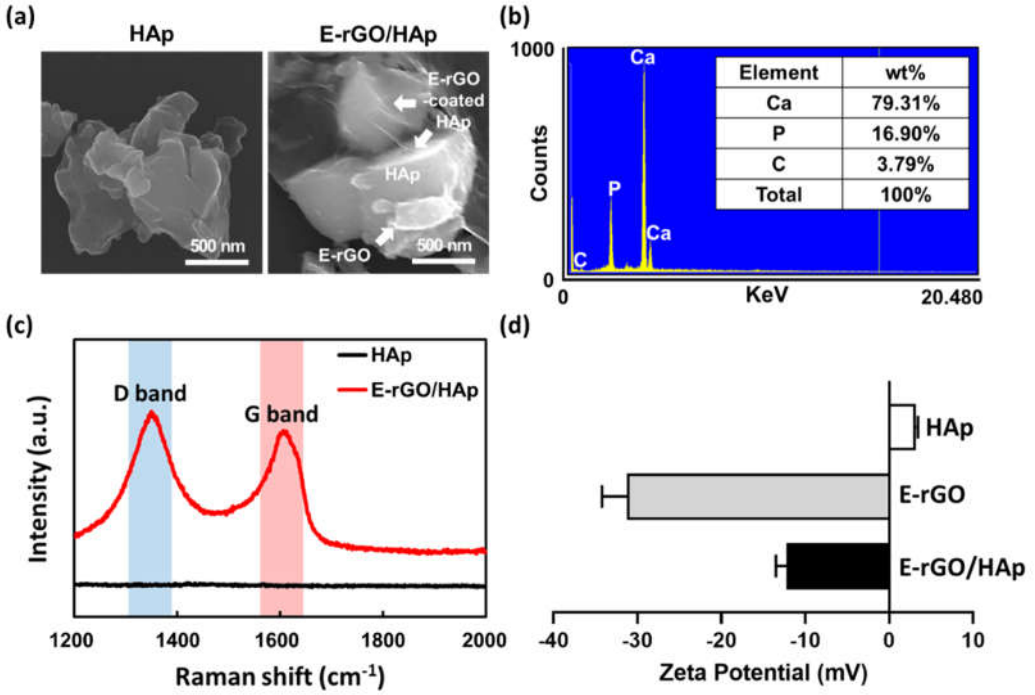

Figure 3. Physicochemical characterization of E-rGO/HAp compared to HAp. (a) SEM images of HAp and E-rGO/HAp, and (b) quantification of EDS map on E-rGO/HAp. (c) Raman spectra of HAp and E-rGO/HAp. (d) Zeta potential measurement of HAp, E-rGO, and E-rGO/HAp.

The effectiveness of E-rGO conjugation with HAp was assessed using Raman spectroscopy of HAp and E-rGO/HAp composites (Fig. 3c). The Raman peaks at 1350 and 1610 cm^{-1} observed in the E-rGO/HAp composites are characteristic of carbon nanomaterials, specifically the D band (~1350 cm^{-1}) and G band (~1600 cm^{-1}) [48, 49]. The G band indicates hybrid carbon from graphene, while the D band arises from structural defects from sp^2 hybrid carbon [50]. The I_D/I_G intensity ratio was found to be 1.11, suggesting that carbon nanomaterial is rGO and its original chemical characteristics was retained [51]. The zeta potential analysis of surface potentials shows that E-rGO in DI water (pH 7.0) were charged at about −32.1 mV, whereas HAp microparticles were charged at about +4.3 mV (Fig. 3d). It was shown that E-rGO was negatively charged over a very wide pH range (0.5–10.0) and their zeta potential fluctuated between −30 mV and −25 mV after 6 h of hydrazine reduction or longer at pH 7.0 [52]. A zeta potential >30 mV (absolute value) is generally regarded as a critical value that represents sufficient mutual repulsion to guarantee the stability of a dispersion [53]. The surface charge of E-rGO/HAp composites was measured to be around −13.6 mV. These results indicate that E-rGO/HAp composites were formed via electrostatic interactions between HAp particles and E-rGO.

Maintaining active proliferation of stem cells is crucial for bone tissue engineering scaffolds. To assess the proliferation of hMSCs, cells were cultured with HAp, E-rGO, and E-rGO/HAp for 5 days (Fig. 4a). After 3 days, the cell proliferation in the HAp group was significantly reduced (77%)

Preprints (www.preprints.org) | NOT PEER-REVIEWED | Posted: 3 May 2023 doi:10.20944/preprints202305.0126.v1

compared to the control group, while there were no significant differences in the E-rGO and E-rGO/HAp groups. However, after 5 days, the proliferation of the E-rGO and E-rGO/HAp groups was significantly increased (112% and 110%, respectively) compared to the control group. Therefore, it is demonstrated that HAp can decrease the early cell proliferation of hMSCs, but the addition of E-rGO can not only mitigate this effect but also increase cell proliferation at longer culture periods. Osteoblasts synthesize and secrete type I collagen, ALP, and other enzymes that regulate mineral deposition, leading to the formation of hydroxyapatite crystals and the mineralization of bone tissue [54]. To compare the ability of HAp, E-rGO, and E-rGO/HAp to promote osteogenic differentiation, the ALP activity of hMSCs was assessed in Figure 4b. All groups showed the highest ALP activity at 14 days, which tended to decrease at 21 days. This is consistent with the observation that ALP is an early osteogenesis marker and is predominantly expressed during hMSCs differentiation into osteogenic lineages [55]. In particular, the hMSCs in the E-rGO and E-rGO/HAp groups showed increased ALP activity at 14 and 21 days compared to the control and HAp groups. Furthermore, the ALP activity of the E-rGO/HAp group was significantly increased compared to the HAp group (164% at day 14 and 152% at day 21), indicating the synergistic osteogenic effects of E-rGO and HAp.

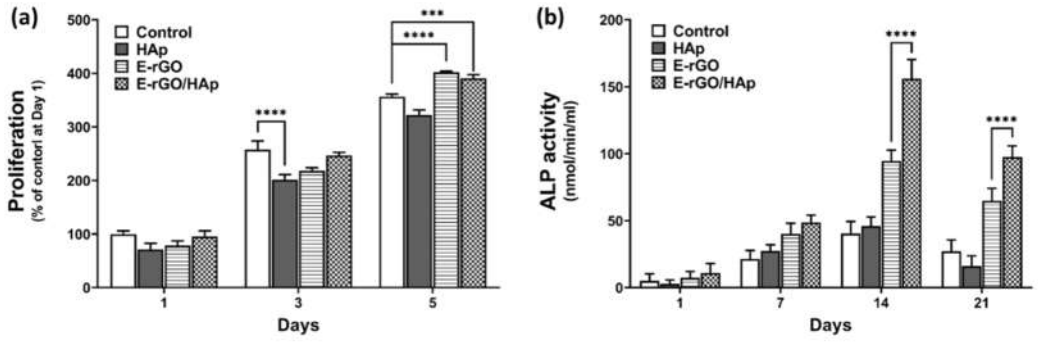

Figure 4. Effects of E-rGO/HAp composites on proliferation and ALP activity of hMSCs. (a) Proliferation of hMSCs cultured with HAp, E-rGO, and E-rGO/HAp. (b) ALP activity of hMSCs cultured with HAp, E-rGO, and E-rGO/HAp. The asterisks represent statistical differences between groups (***$p < 0.001$ and ****$p < 0.0001$).

To further explore the osteogenic differentiation-inducing effect of E-rGO/HAp composites, calcium phosphate deposition which is considered as a later marker for bone regeneration was observed by ARS staining. The image of ARS staining (Fig. 5a) and its quantification (Fig. 5b) showed that E-rGO and E-rGO/HAp groups showed increased mineralization nodule formation compared to control. Furthermore, mineralization nodule formation of the E-rGO/HAp group was significantly increased compared to the E-rGO group (129% at day 14 and 171% at day 21), suggesting E-rGO can induce an osteoid matrix deposition even without any osteogenic inducing agents.

Preprints (www.preprints.org) | NOT PEER-REVIEWED | Posted: 3 May 2023 doi:10.20944/preprints202305.0126.v1

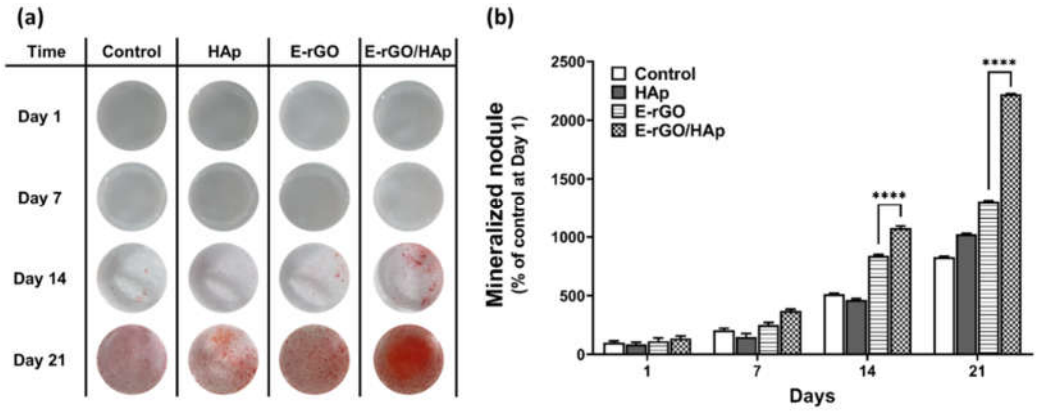

Figure 5. Effects of E-rGO/HAp composites on calcium deposition and matrix mineralization in hMSCs. (a) digital images of ARS staining and (b) quantification of mineralized nodule formation on hMSCs cultured with HAp, E-rGO, and E-rGO/HAp. The asterisks represent statistical differences between groups (****$p < 0.0001$).

Numerous studies have demonstrated the osteogenic effects of HAp derived from unique aspects of the material [56, 57]. Some studies attribute HAp's osteogenic effects to geometric factors, such as the micropores in HAp ceramics that connect macropores, permitting interstitial fluid flow through the matrix [58]. At the initial stage of cell adhesion, the surface of HAp can affect gene expression, and signal transduction pathways depend on the attachment of stem cells to HAp surfaces [59]. This attachment leads to the sequential expression of integrins, FAK, and ERK genes required for cell attachment, followed by the expression of proliferative genes, c-jun and c-fos gene, culminating in the expression of the ALP gene during the differentiation stage [60]. Despite its potential as a cell scaffold, HAp has some drawbacks, such as low electrical conductivity and brittleness. To address these limitations, reduced graphene oxide (rGO) can be added to HAp scaffolds to enhance their electrical conductivity, which in turn allows adsorption of serum proteins and growth factors to the scaffold's numerous surface functional groups, such as hydroxyl, epoxy, carbonyl, and carboxyl groups [61]. This effect increases the local concentration of proteins and osteogenic inducers on the scaffold surface, which are then available for stem cells. The microporous structures and structural defects of the resulting E-rGO/HAp composites are suggested to benefit the growth and osteogenic differentiation of stem cells by providing an extracellular matrix (ECM) biomimetic microenvironment [62]. Furthermore, the addition of rGO to HAp scaffolds improves their mechanical strength, which promises greater opportunity for orthopedic applications [63]. Therefore, we suggest that the addition of E-rGO to HAp scaffolds enhances their osteogenic differentiation-inducing effect, supporting early and late osteogenic differentiation of hMSCs. This approach provides a promising strategy for addressing the low electrical conductivity and brittleness of HAp, while also offering improved mechanical strength and a biomimetic microenvironment for growth and osteogenic differentiation of hMSCs.

4. Conclusions

To summarize, we introduced environmentally friendly and cost-effective methods for synthesizing E-rGO and Tuna-derived HAp. E-rGO was reduced using green tea extract EGCG, while HAp powder was obtained from Atlantic bluefin tuna (*Thunnus thynnus*). The physicochemical analysis indicated that the E-rGO/HAp composites had exceptional chemical properties for use as tissue engineering scaffolds, as well as high purity. Moreover, we discovered that culturing hMSCs with E-rGO/HAp composites induced spontaneous osteogenic differentiation. However, more detailed mechanism involving intracellular signaling pathways remains obscure and requires further study at the molecular level. Nonetheless, our work suggests that E-rGO/HAp composites may play a significant role in promoting the spontaneous osteogenic differentiation of hMSCs, and we envision that these E-rGO-based composites could serve as promising candidates for tissue engineering

 doi:10.20944/preprints202305.0126.v1

scaffolds, stem cell differentiation stimulators, and implantable device components due to their biocompatible and bioactive properties.

Author Contributions: Formal analysis, Investigation, Methodology, Writing – Original Draft, M.S.K., R.P.; Data curation, Software, Visualization, H.J.J., Y.C.S., C.-S.K.; Resources, Validation, S.-H.H.; Conceptualization, Funding acquisition, Project administration, Supervision, Writing – Review & Editing, S.W.H., J.O., D.-W.H. All authors have read and agreed to the published version of the manuscript.

Funding: This research was funded by National Research Foundation of Korea (NRF) grant funded by the Korea government (MSIT) (No. 2021R1A2C2006013) and the Korea Evaluation Institute of Industrial Technology (KEIT) grant funded by the Ministry of Trade, Industry, and Energy (MOTIE, Korea) (No. 20014399).

Institutional Review Board Statement: Not applicable.

Informed Consent Statement: Not applicable.

Data Availability Statement: All data needed to evaluate the conclusions in the paper are present in the paper. Additional data related to this paper may be requested from the authors.

Acknowledgments: Not applicable.

Conflicts of Interest: The authors declare no conflict of interest.

References

1. Kang, M.S.; Jeong, S.J.; Lee, S.H.; Kim, B.; Hong, S.W.; Lee, J.H.; Han, D.-W. Reduced graphene oxide coating enhances osteogenic differentiation of human mesenchymal stem cells on Ti surfaces. *Biomater Res* **2021**, 25, 1–9.
2. Wu, Y.; Li, M.; Su, H.; Chen, H.; Zhu, Y. Up-to-date progress in bioprinting of bone tissue. *Int J Bioprint* **2022**, 9, 628.
3. Khan, S.N.; Cammisa Jr, F.P.; Sandhu, H.S.; Diwan, A.D.; Girardi, F.P.; Lane, J.M. The biology of bone grafting. *J Am Acad Orthop Surg* **2005**, 13, 77–86.
4. Balhuc, S.; Campian, R.; Labunet, A.; Negucioiu, M.; Buduru, S.; Kui, A. Dental applications of systems based on hydroxyapatite nanoparticles—an evidence-based update. *Crystals* **2021**, 11, 674.
5. Chandra, G.; Pandey, A. Biodegradable bone implants in orthopedic applications: a review. *Biocybern Biomed Eng* **2020**, 40, 596–610.
6. Kao, C.-Y.; Lin, T.-L.; Lin, Y.-H.; Lee, A.K.-X.; Ng, S.Y.; Huang, T.-H.; Hsu, T.-T. Synergistic effect of static magnetic fields and 3D-printed iron-oxide-nanoparticle-containing calcium silicate/poly-ε-caprolactone scaffolds for bone tissue engineering. *Cells* **2022**, 11, 3967.
7. Wang, C.; Gao, S.; Lu, R.; Wang, X.; Chen, S. In vitro and in vivo studies of hydrogenated titanium dioxide nanotubes with superhydrophilic surfaces during early osseointegration. *Cells* **2022**, 11, 3417.
8. Aghali, A. Craniofacial bone tissue engineering: current approaches and potential therapy. *Cells* **2021**, 10, 2993.
9. Mobasherpour, I.; Heshajin, M.S.; Kazemzadeh, A.; Zakeri, M. Synthesis of nanocrystalline hydroxyapatite by using precipitation method. *J Alloys and Comp* **2007**, 430, 330–333.
10. Ebrahimi, S.; Nasri, C.S.S.M., Arshad, S.E.B. Hydrothermal synthesis of hydroxyapatite powders using Response Surface Methodology (RSM). *PloS One* **2021**, 16, e0251009.
11. Fathi, M.; Zahrani, E.M. Mechanical alloying synthesis and bioactivity evaluation of nanocrystalline fluoridated hydroxyapatite. *J Crystal Growth* **2009**, 311, 1392–1403.
12. Yeong, K.; Wang, J.; Ng, S. Mechanochemical synthesis of nanocrystalline hydroxyapatite from CaO and $CaHPO_4$. *Biomaterials* **2001**, 22, 2705–2712.
13. Tseng, Y.-H.; Kuo, C.-S.; Li, Y.-Y.; Huang, C.-P. Polymer-assisted synthesis of hydroxyapatite nanoparticle. *Mater Sci Eng C* **2009**, 29, 819–822.
14. Simon, V.; Lazăr, D.; Turcu, R.; Mocuta, H.; Magyari, K.; Prinz, M.; Neumann, M.; Simon, S. Atomic environment in sol–gel derived nanocrystalline hydroxyapatite. *Mater Sci Eng B* **2009**, 165, 247–251.
15. Park, S.J.; Gupta, K.C.; Kim, H.; Kim, S.; Kang, I.-K. Osteoblast behaviours on nanorod hydroxyapatite-grafted glass surfaces. *Biomater Res* **2019**, 23, 28.
16. Kim, C.; Lee, J.W.; Heo, J.H.; Park, C.; Kim, D.-H.; Yi, G.S.; Kang, H.C.; Jung, H.S.; Shin, H.; Lee, J.H. Natural bone-mimicking nanopore-incorporated hydroxyapatite scaffolds for enhanced bone tissue regeneration. *Biomater Res* **2022**, 26, 7.
17. Jeong, J.; Kim, J.H.; Shim, J.H.; Hwang, N.S.; Heo, C.Y. Bioactive calcium phosphate materials and applications in bone regeneration. *Biomater Res* **2019**, 23, 4.
18. Akram, M.; Ahmed, R.; Shakir, I.; Ibrahim, W.A.W.; Hussain, R. Extracting hydroxyapatite and its precursors from natural resources. *J Mater Sci* **2014**, 49, 1461–1475.

19. Ronan, K.; Kannan, M.B. Novel sustainable route for synthesis of hydroxyapatite biomaterial from biowastes. *ACS Sustainable Chem Eng* **2017**, 5, 2237–2245.
20. Gergely, G.; Wéber, F.; Lukács, I.; Tóth, A.L.; Horváth, Z.E.; Mihály, J.; Balázsi, C. Preparation and characterization of hydroxyapatite from eggshell. *Ceram Int* **2010**, 36, 803–806.
21. Sivakumar, M.; Kumar, T.S.; Shantha, K.; Rao, K.P. Development of hydroxyapatite derived from Indian coral. *Biomaterials* **1996**, 17, 1709–1714.
22. Mondal, B.; Mondal, S.; Mondal, A.; Mandal, N. Fish scale derived hydroxyapatite scaffold for bone tissue engineering. *Mater Charact* **2016**, 121, 112–124.
23. Barakat, N.A.; Khil, M.S.; Omran, A.; Sheikh, F.A.; Kim, H.Y. Extraction of pure natural hydroxyapatite from the bovine bones bio waste by three different methods. *J Mater Process Technol* **2009**, 209, 3408–3415.
24. Qiao, W.; Liu, Q.; Li, Z.; Zhang, H.; Chen, Z. Changes in physicochemical and biological properties of porcine bone derived hydroxyapatite induced by the incorporation of fluoride. *Sci Technol Adv Mater* **2017**, 18, 110–121.
25. Jongjareonrak, A.; Benjakul, S.; Visessanguan, W.; Nagai, T.; Tanaka, M. Isolation and characterisation of acid and pepsin-solubilised collagens from the skin of Brownstripe red snapper (*Lutjanus vitta*). *Food Chem* **2005**, 93, 475–484.
26. Paul, S.; Pal, A.; Choudhury, A.R.; Bodhak, S.; Balla, V.K.; Sinha, A.; Das, M. Effect of trace elements on the sintering effect of fish scale derived hydroxyapatite and its bioactivity. *Ceram Int* **2017**, 43, 15678–15684.
27. Culurgioni, J.; Mele, S.; Merella, P.; Addis, P.; Figus, V.; Cau, A.; Karakulak, F.S.; Garippa, G. Metazoan gill parasites of the Atlantic bluefin tuna *Thunnus thynnus* (Linnaeus) (Osteichthyes: Scombridae) from the Mediterranean and their possible use as biological tags. *Folia Parasitol* **2014**, 61, 148.
28. Venkatesan, J.; Kim, S.K. Effect of temperature on isolation and characterization of hydroxyapatite from tuna (*Thunnus obesus*) bone. *Materials* **2010**, 3, 4761–4772.
29. Li, Q.; Feng, C.; Cao, Q.; Wang, W.; Ma, Z.; Wu, Y.; He, T.; Jing, Y.; Tan, W.; Liao, T. Strategies of strengthening mechanical properties in the osteoinductive calcium phosphate bioceramics. *Regen Biomater* **2023**, rbad013.
30. Han, D.-W.; Hong, S.W. *Multifaceted Biomedical Applications of Graphene*, 1st ed.; Springer: Singapore, 2022; pp. 1–264.
31. Lee, J.H.; Shin, Y.C.; Jin, O.S.; Kang, S.H.; Hwang, Y.-S.; Park, J.-C.; Hong, S.W.; Han, D.-W. Reduced graphene oxide-coated hydroxyapatite composites stimulate spontaneous osteogenic differentiation of human mesenchymal stem cells. *Nanoscale* **2015**, 7, 11642–11651.
32. Shin, Y.C.; Bae, J.-H.; Lee, J.H.; Raja, I.S.; Kang, M.S.; Kim, B.; Hong, S.W.; Huh, J.-B.; Han, D.-W. Enhanced osseointegration of dental implants with reduced graphene oxide coating. *Biomater Res* **2022**, 26, 11.
33. Shin, Y.C.; Lee, J.H.; Jin, O.S.; Kang, S.H.; Hong, S.W.; Kim, B.; Park, J.-C.; Han, D.-W. Synergistic effects of reduced graphene oxide and hydroxyapatite on osteogenic differentiation of MC3T3-E1 preosteoblasts. *Carbon* **2015**, 95, 1051–1060.
34. Raja, I.S.; Preeth, D.R.; Vedhanayagam, M.; Hyon, S.-H.; Lim, D.; Kim, B.; Rajalakshmi, S.; Han, D.-W. Polyphenols-loaded electrospun nanofibers in bone tissue engineering and regeneration. *Biomater Res* **2021**, 25, 29.
35. Hao, L.; Song, H.; Zhan, Z.; Lv, Y. Multifunctional reduced graphene oxide-based nanoplatform for synergistic targeted chemo-photothermal therapy. *ACS Appl Bio Mater* **2020**, 3, 5213–5222.
36. Wang, Y.; Shi, Z.; Yin, J. Facile synthesis of soluble graphene via a green reduction of graphene oxide in tea solution and its biocomposites. *ACS Appl Mater Interfaces* **2011**, 3, 1127–1133.
37. Chandrasekar, A.; Sagadevan, S.; Dakshnamoorthy, A. Synthesis and characterization of nano-hydroxyapatite (n-HAP) using the wet chemical technique. *Int J Phys Sci* **2013**, 8, 1639–1645.
38. Mathirat, A.; Dalavi, P.A.; Prabhu, A.; GV, Y.D.; Anil, S.; Senthilkumar, K.; Seong, G.H.; Sargod, S.S.; Bhat, S.S.; Venkatesan, J. Remineralizing potential of natural nano-hydroxyapatite obtained from epinephelus chlorostigma in artificially induced early enamel lesion: an in vitro study. *Nanomaterials* **2022**, 12, 3993.
39. Bouyer, E.; Gitzhofer, F.; Boulos, M. Morphological study of hydroxyapatite nanocrystal suspension. *J Mater Sci Mater Med* **2000**, 11, 523–531.
40. Leal-Egaña, A.; Díaz-Cuenca, A.; Boccaccini, A.R. Tuning of cell–biomaterial anchorage for tissue regeneration. *Adv Mater* **2013**, 25, 4049–4057.
41. Gross, K.A.; Gross, V.; Berndt, C.C. Thermal analysis of amorphous phases in hydroxyapatite coatings. *J Am Ceram Soc* **1998**, 81, 106–112.
42. Liao, C.-J.; Lin, F.-H.; Chen, K.-S.; Sun, J.-S. Thermal decomposition and reconstitution of hydroxyapatite in air atmosphere. *Biomaterials* **1999**, 20, 1807–1813.
43. Capanema, N.S.; Mansur, A.A.; Carvalho, S.M.; Silva, A.R.; Ciminelli, V.S.; Mansur, H.S. Niobium-doped hydroxyapatite bioceramics: synthesis, characterization and in vitro cytocompatibility. *Materials* **2015**, 8, 4191–4209.
44. Miculescu, F.; Antoniac, I.; Ciocan, L.T.; Miculescu, M.; Brânzei, M.; Ernuteanu, A.; Batalu, D.; Berbecaru, A. Complex analysis on heat treated human compact bones. *UPB Sci Bull B* **2011**, 73, 203–211.

45. Amirthalingam, N.; Deivarajan, T.; Paramasivam, M. Mechano chemical synthesis of hydroxyapatite using dolomite. *Mater Lett* **2019**, 254, 379–382.
46. Wang, H.; Lee, J.K.; Moursi, A.; Lannutti, J.J. Ca/P ratio effects on the degradation of hydroxyapatite in vitro. *J Biomed Mater Res A* **2003**, 67, 599–608.
47. Liu, H.; Yazici, H.; Ergun, C.; Webster, T.J.; Bermek, H. An in vitro evaluation of the Ca/P ratio for the cytocompatibility of nano-to-micron particulate calcium phosphates for bone regeneration. *Acta Biomater* **2008**, 4, 1472–1479.
48. Shin, M.C.; Kang, M.S.; Park, R.; Chae, S.Y.; Han, D.-W.; Hong, S.W. Differential cellular interactions and responses to ultrathin micropatterned graphene oxide arrays with or without ordered in turn RGD peptide films. *Appl Surf Sci* **2021**, 561, 150115.
49. Park, K.O.; Lee, J.H.; Park, J.H.; Shin, Y.C.; Huh, J.B.; Bae, J.-H.; Kang, S.H.; Hong, S.W.; Kim, B.; Yang, D.J. Graphene oxide-coated guided bone regeneration membranes with enhanced osteogenesis: Spectroscopic analysis and animal study. *Appl Spectrosc Rev* **2016**, 51, 540–551.
50. Kang, M.S.; Kang, J.I.; Le Thi, P.; Park, K.M.; Hong, S.W.; Choi, Y.S.; Han, D.-W.; Park, K.D. Three-dimensional printable gelatin hydrogels incorporating graphene oxide to enable spontaneous myogenic differentiation. *ACS Macro Lett* **2021**, 10, 426–432.
51. Tang, B.; Guoxin, H.; Gao, H. Raman spectroscopic characterization of graphene. *Appl Spectrosc Rev* **2010**, 45, 369–407.
52. Li, M.-j.; Liu, C.-m.; Xie, Y.-b.; Cao, H.-b.; Zhao, H.; Zhang, Y. The evolution of surface charge on graphene oxide during the reduction and its application in electroanalysis. *Carbon* **2014**, 66, 302-311.
53. Everett, D.H. *Basic Principles of Colloid Science*, 1st ed.; Royal Society of Chemistry: London, UK, 2007; pp. 1–243.
54. Blair, H.C.; Larrouture, Q.C.; Li, Y.; Lin, H.; Beer-Stoltz, D.; Liu, L.; Tuan, R.S.; Robinson, L.J.; Schlesinger, P.H.; Nelson, D.J. Osteoblast differentiation and bone matrix formation in vivo and in vitro. *Tissue Eng B* **2017**, 23, 268–280.
55. Wrobel, E.; Leszczynska, J.; Brzoska, E. The characteristics of human bone-derived cells (HBDCS) during osteogenesis in vitro. *Cell Mol Biol Lett* **2016**, 21, 1–15.
56. Yang, X.; Li, Y.; Liu, X.; Zhang, R.; Feng, Q. In vitro uptake of hydroxyapatite nanoparticles and their effect on osteogenic differentiation of human mesenchymal stem cells. *Stem Cells Int* **2018**, 2018.
57. Zhao, Y.; Chen, H.; Ran, K.; Zhang, Y.; Pan, H.; Shangguan, J.; Tong, M.; Yang, J.; Yao, Q.; Xu, H. Porous hydroxyapatite scaffold orchestrated with bioactive coatings for rapid bone repair. *Biomater Adv* **2023**, 144, 213202.
58. Yang, W.; Han, W.; He, W.; Li, J.; Wang, J.; Feng, H.; Qian, Y. Surface topography of hydroxyapatite promotes osteogenic differentiation of human bone marrow mesenchymal stem cells. *Mater Sci Eng C* **2016**, 60, 45–53.
59. Lin, L.; Chow, K.L.; Leng, Y. Study of hydroxyapatite osteoinductivity with an osteogenic differentiation of mesenchymal stem cells. *J Biomed Mater Res A* **2009**, 89, 326–335.
60. Liu, L.; Gao, X.; Li, X.; Zhu, G.; Li, N.; Shi, X.; Wang, Y. Calcium alendronate-coated composite scaffolds promote osteogenesis of ADSCs via integrin and FAK/ERK signalling pathways. *J Mater Chem B* **2020**, 8, 6912–6924.
61. Li, H.; Fierens, K.; Zhang, Z.; Vanparijs, N.; Schuijs, M.J.; Van Steendam, K.; Feiner Gracia, N.; De Rycke, R.; De Beer, T.; De Beuckelaer, A. Spontaneous protein adsorption on graphene oxide nanosheets allowing efficient intracellular vaccine protein delivery. *ACS Appl Mater Interfaces* **2016**, 8, 1147–1155.
62. Lee, J.H.; Shin, Y.C.; Lee, S.-M.; Jin, O.S.; Kang, S.H.; Hong, S.W.; Jeong, C.-M.; Huh, J.B.; Han, D.-W. Enhanced osteogenesis by reduced graphene oxide/hydroxyapatite nanocomposites. *Sci Rep* **2015**, 5, 18833.
63. Zhou, K.; Yu, P.; Shi, X.; Ling, T.; Zeng, W.; Chen, A.; Yang, W.; Zhou, Z. Hierarchically porous hydroxyapatite hybrid scaffold incorporated with reduced graphene oxide for rapid bone ingrowth and repair. *ACS Nano* **2019**, 13, 9595–9606.